Magnetosheath Jets and Plasmoids: Characteristics and Formation Mechanisms from Hybrid Simulations

Luis Preisser[1] , Xóchitl Blanco-Cano[1] , Primoz Kajdič[1] , David Burgess[2] , and Domenico Trotta[2]
[1] Instituto de Geofísica UNAM Circuito de la Investigación Científica s/n, Coyoacán 04510, Mexico City, Mexico; preisser@igeofisica.unam.mx
[2] School of Physics and Astronomy, Queen Mary University of London London E1 4NS, UK

Abstract

Magnetosheath jets and plasmoids are very common phenomena downstream of Earth's quasi-parallel bow shock. As the increase of the dynamic pressure is one of the principal characteristics of magnetosheath jets, the embedded paramagnetic plasmoids have been considered as an special case of the former. Although the properties of both types of structures have been widely studied during the last 20 years, their formation mechanisms have not been examined thoroughly. In this work we perform a 2D local hybrid simulation (kinetic ions – fluid electrons) of a quasi-parallel ($\theta_{Bn} = 15°$), supercritical ($M_A = 7$) collisionless shock in order to study these mechanisms. Specifically, we analyze the formation of one jet and one plasmoid, showing for the first time that they can be produced by different mechanisms related to the same shock. In our simulation, the magnetosheath jet is formed according to the mechanism proposed by Hietala, where at the shock ripples the upstream solar wind suffers locally less deceleration and the flow is focused in the downstream side, producing a compressed and high-velocity region that leads to an increase of dynamic pressure downstream of the shock. The formation of the plasmoid, however, follows a completely new scenario being generated by magnetic reconnection between two plasma layers with opposite B-field orientation in the region just behind the shock.

1. Introduction

When the super-magnetosonic solar wind (SW) encounters the Earth's bow shock, it is decelerated to sub-magnetosonic speeds (e.g., Tsurutani & Stone 1985; Burgess 1995; Burgess & Scholer 2015). Due to its collisionless nature, the bow shock is strongly rippled especially where its geometry, characterized by the angle θ_{Bn} between the shock's local normal and the upstream interplanetary magnetic field, is quasi-parallel ($\theta_{Bn} < 45°$, e.g., Burgess 1989; Krauss-Varban & Omidi 1991; Schwartz & Burgess 1991; Blanco-Cano et al. 2009). Downstream of the bow shock there is a region called the magnetosheath (Lucek et al. 2005), which, in the case of a quasi-parallel bow shock, is populated by strong B-field and plasma fluctuations. Most of the time the observed fluctuations are either turbulence (Omidi et al. 1994; Shevyrev et al. 2003; Shevyrev & Zastenker 2005; Yordanova et al. 2016; Rakhmanova et al. 2018), ion-cyclotron waves, or mirror-mode fluctuations (e.g., Schwartz et al. 1996, and references therein).

There is another type of structures in the magnetosheath, commonly called magnetosheath jets (Plaschke et al. 2018, and references therein). These jets were first described by Němeček et al. (1998) as transient and local ion flux enhancements. Later, they were more commonly defined as enhancements of dynamic pressure (P_{dyn}, Archer et al. 2012; Hietala et al. 2012; Archer & Horbury 2013; Savin et al. 2014), increments in dynamic pressure calculated with only the V_x component ($P_{dyn,x}$, Plaschke et al. 2013) and changes in plasma velocity (Hietala et al. 2012; Gunell et al. 2014). Because the identification of an

enhancement requires a threshold, some authors have used values calculated with respect to the background magnetosheath plasma (e.g., Archer & Horbury 2013) while others use upstream SW properties (e.g., Amata et al. 2011; Plaschke et al. 2013).

In order to study the jet formation mechanism triggered for upstream conditions, in this work we will consider as a jet any structure that fulfills the following identification conditions adapted from Plaschke et al. (2013) and illustrated in Figure 1(a).

1. Within a jet $P_{dyn,x,jet} \geqslant 0.5\, P_{dyn,x,up}$, where $P_{dyn,x,jet}$ and $P_{dyn,x,up}$ are values inside the jet and upstream of the bow shock.
2. The jet interval is delimited by the condition $P_{dyn,x,jet} \geqslant 0.25\, P_{dyn,x,up}$.
3. Before and after the jet interval the condition $V_{x,down} \geqslant 0.5\, V_{x,down}(t_0)$ must be satisfied (t_0 is the time of the peak in $P_{dyn,x,jet}$). This ensures velocity enhancements confined to the respective jet interval, and not simply density enhancements within a steady flow.
4. V_x throughout the jet is negative (anti-sunward propagation).

In addition to its characterization (see Tables 1 and 2 in Plaschke et al. 2018), different formation mechanisms have been proposed for magnetosheath jets. Hietala et al. (2009) suggested that jets are formed at bow-shock ripples. The idea is that at these ripples, the incoming SW plasma is locally decelerated less than the surrounding plasma being focused and additionally compressed in the downstream region leading to a local increase of P_{dyn} observed in the magnetosheath. Archer et al. (2012) linked jets to upstream rotational discontinuities transmitted to the magnetosheath region, while Savin et al. (2012) associated them to hot flow anomalies (e.g., Lucek et al. 2004; Omidi & Sibeck 2007). In a recent work using an hybrid simulation
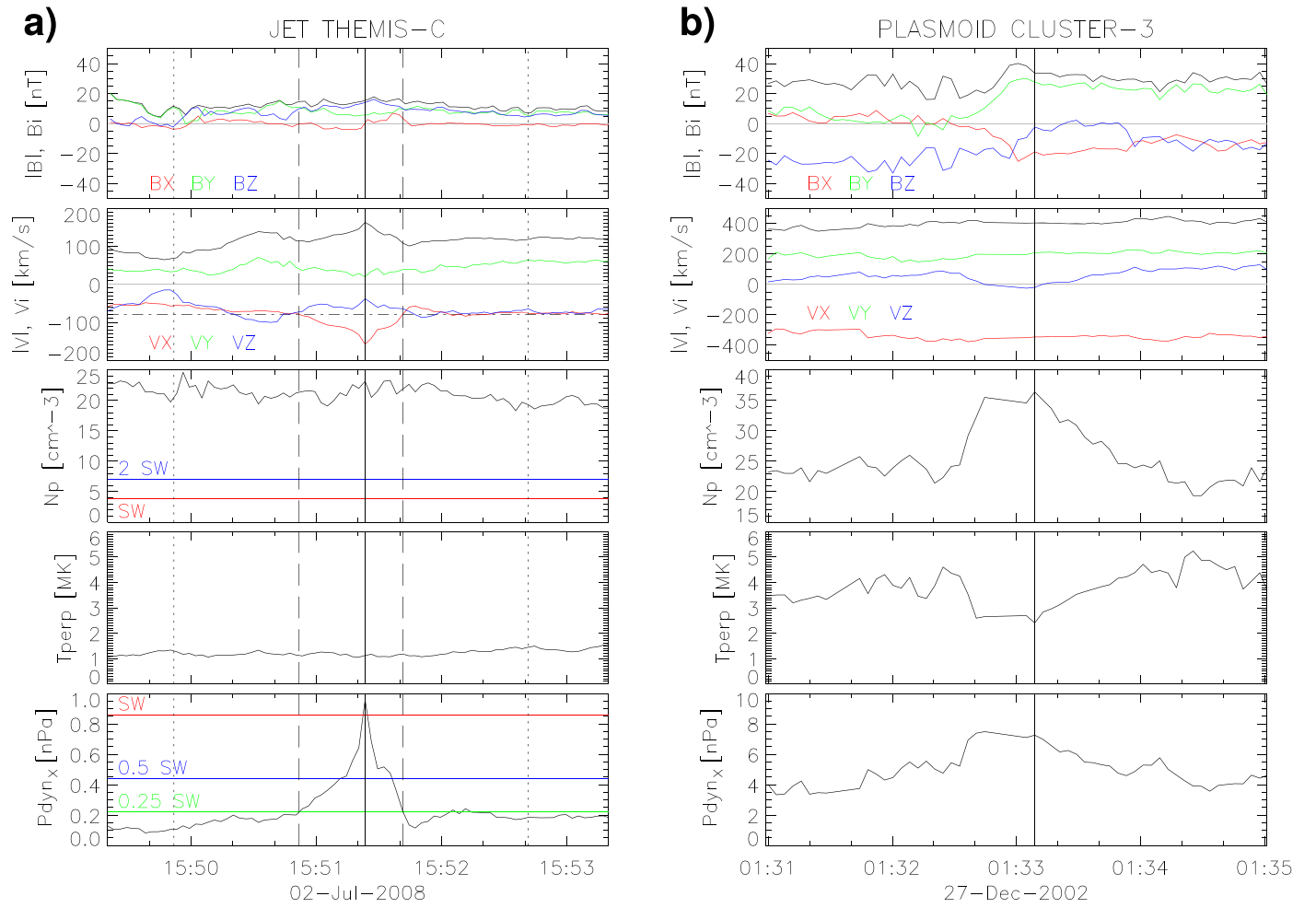
Figure 1. (a) Jet observed by THEMIS-C (adapted from Plaschke et al. 2013). (b) Paramagnetic embedded plasmoid observed by CLUSTER-3 (adapted from Karlsson et al. 2015). From top to bottom, magnetic field and bulk velocity measurements in GSE coordinates, ion density, perpendicular ion temperature and $P_{dyn,x}$.

Hao et al. (2016a) show how a magnetic filamentary structure with high P_{dyn} is formed downstream of a 30° quasi-parallel shock.

On the other hand, closely related structures called plasmoids have been studied from a different point of view, in the form of density enhancements over the background values without any a priori connection to an increase in the flow velocity (e.g., Hubert & Harvey 2000; Karlsson et al. 2012, 2015; Gutynska et al. 2015). In a statistical study Karlsson et al. (2012) found that all of them were associated with magnetic field rotation and an increase or decrease of B-magnitude. Karlsson et al. (2015) showed that two distinct categories of plasmoids can exist. The first category with a diamagnetic signature (decrease in B-field magnitude) is found in both SW and magnetosheath regions. The second plasmoid population were only found in the magnetosheath, exhibiting a paramagnetic signature (increase in magnetic field magnitude) and they could have (or not have) an associated increase in velocity.

Focusing on the latter, here we consider a paramagnetic embedded plasmoid to be any magnetosheath structure that satisfies the following criteria (based on Karlsson et al. 2015) and also illustrated with an observational case in Figure 1(b).

1. Localized ion density enhancement of 30% over the average ambient value.

2. Increment in B-magnitude between 0% and 50% above the average, accompanied by a change in direction of at least one of the magnetic components.
3. Bulk velocity enhancements of $\leqslant 10\%$ compared to ambient values.
4. Decrement in perpendicular temperature $T_\perp$.

For the generation of magnetosheath plasmoids Karlsson et al. (2012) proposed that diamagnetic plasmoids from the pristine SW can be transmitted into the magnetosheath, while the paramagnetic plasmoids could be formed when short, large-amplitude magnetic structures (SLAMS; Schwartz et al. 1992; Giacalone et al. 1993; Dubouloz & Scholer 1995; Tsubouchi & Lembège 2004) cross from the foreshock (Eastwood et al. 2005) into the magnetosheath.

As pointed out by Karlsson et al. (2015), a comparison of the properties of jets and plasmoids is of great interest as it could help to determine whether or not their generation mechanisms are the same. Following these arguments, here we study via local hybrid simulations jets and plasmoids as entities with different signatures, showing for the first time that they can be formed by the same shock but by two different mechanisms. For the plasmoid we show for the first time that its formation is related to magnetic reconnection in the region just behind the shock.
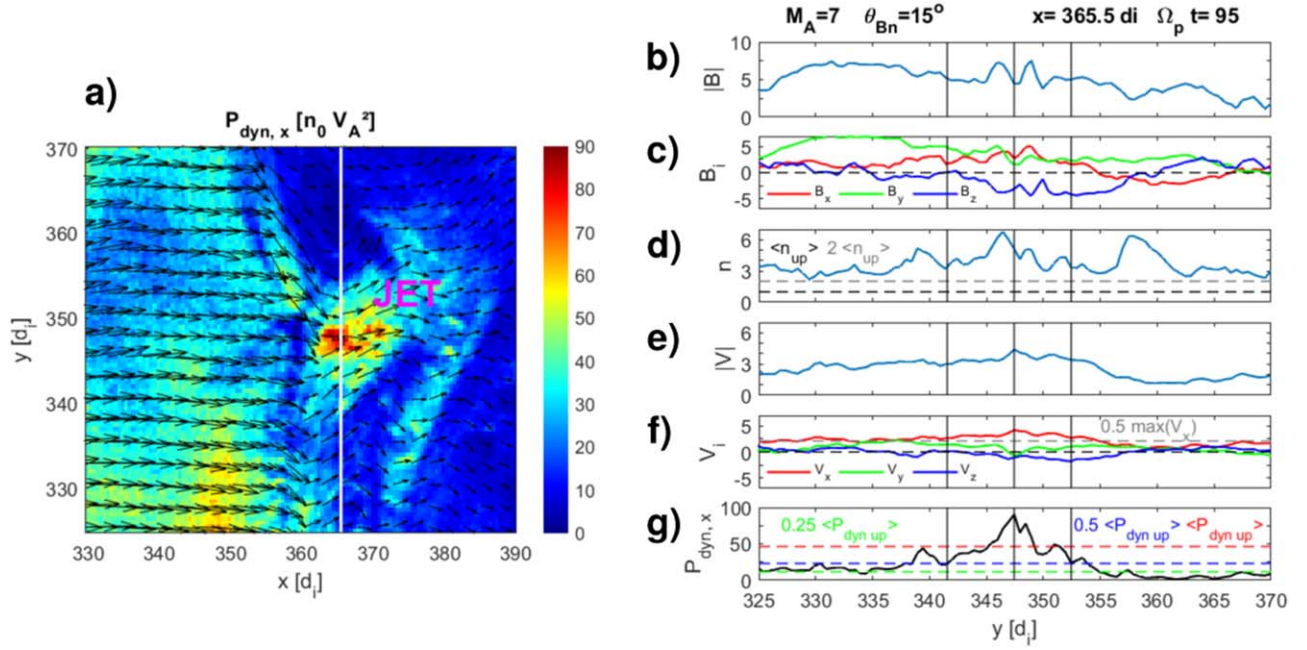
Figure 2. (a) $P_{\mathrm{dyn},x}$ in colors and bulk velocity (vectors) at $\Omega_p\, t = 365.5$. The white line indicates the cut through the jet along which the following spatial profile parameters are plotted: (b) magnetic field magnitude, (c) B-field components, (d) ion density (the horizontal black and gray lines correspond to the upstream value n and $n/2$ respectively), (e) ion bulk velocity, (f) velocity components (the value corresponding to half the maximum of V_x inside the jet is indicated with the gray horizontal line), and (g) $P_{\mathrm{dyn},x}$ (averaged upstream values corresponding to $P_{\mathrm{dyn},x}$, $P_{\mathrm{dyn},x}/2$ and $P_{\mathrm{dyn},x}/4$ are indicated in red, blue, and green lines). The central vertical line on panels (b)–(g) marks the maximum of $P_{\mathrm{dyn},x}$ while the left and the right vertical lines delimit the jet defined as the locations around the $P_{\mathrm{dyn},x}$ maximum where $P_{\mathrm{dyn},x} = 0.5\langle P_{\mathrm{dyn},x}\rangle_{\mathrm{up}}$.

2. Numerical Setup

The simulation was performed using the hybrid particle-In-cell code HYPSI (Burgess & Scholer 2015; Gingell et al. 2017). Under this approach protons are treated kinetically while electrons are considered as a charge-neutralizing massless fluid. Spatial and temporal scales are expressed in units of proton inertial length $d_i = c/\omega_p$ (ω_p is the proton plasma frequency, c is the speed of light) and the inverse of the proton gyrofrequency Ω_p^{-1}, respectively, while the velocity is normalized to the Alfvén speed $V_A = B_{\mathrm{up}}/\sqrt{\mu_o n_o m_p}$. Proton density n_o m_p and magnetic field B_{up} are normalized to the initial upstream values. The number of grid cells is $n_x \times n_y = 1000 \times 800$, with cell sizes of $\Delta x = \Delta y = 0.5\ c/\omega_p$. The time step Δt was chosen so that $\Omega_p\ \Delta t = 0.005$. The velocity, magnetic field, and electric field are 3D vectors. The plasma was initialized with an inflow speed $V_{\mathrm{in}} = 5.5\ V_A$ along the x-direction with the magnetic field in the x–y simulation plane forming an angle (the nominal θ_{Bn}) of 15° with the x-axis. The right boundary of the simulation acts as a perfectly reflecting wall to the plasma that is continuously injected from the left open boundary. The simulation is periodic in the y direction. As a consequence of the interaction between the reflected and injected plasma, a shock propagating in the negative x-direction with a $M_A = 7$ is formed. A finite resistivity, $\eta = 0.06\ \omega_p^{-1}$ is used in the simulations with an isotropic upstream Maxwellian velocity distribution function for protons, and upstream plasma beta (the ratio of kinetic to magnetic pressure) $\beta_p = \beta_e = 0.5$. The initial number of particles per cell is ∼100. In the box simulation frame the shock moves to the left. The velocities and then the dynamic pressure for this work were computed in the shock reference frame.

3. Simulation Results

Our simulation reproduces the inherent and well-known structures of quasi-parallel shocks, such as ripples along the shock surface and fluctuations in plasma parameters on both sides of the shock in agreement with previous simulation works (Burgess 1989; Krauss-Varban & Omidi 1991; Burgess 1995; Hao et al. 2016a, 2016b, 2017). After an inspection of downstream parameters we identified a jet and a paramagnetic embedded plasmoid based on the criteria defined in Section 1.

3.1. Reproducing the Observational Signatures

Figure 2(a) shows an excerpt of the simulation domain at $\Omega_p\, t = 95$. The colors represent $P_{\mathrm{dyn},x}$ while the black arrows show the local direction of the plasma velocity. The rippled shock front is easily identified by the abrupt change in direction of the velocity around $x = 360\ d_i$, which coincides with the change of $P_{\mathrm{dyn},x}$ from ∼35 $n_0 V_A^2$ in the upstream side to ∼15 $n_0 V_A^2$ in the downstream region. Most of the downstream region exhibits low $P_{\mathrm{dyn},x}$ values (blue color) with exception of the region marked as "JET" where large $P_{\mathrm{dyn},x}$ values between 40 and 90 $n_0 V_A^2$ are present. This region extends between $x \sim 355$–380 d_i and $y \sim 340$–355 d_i. This feature is in qualitative agreement with the physical picture of jet generation proposed in Hietala et al. (2009) and Hietala & Plaschke (2013). We analyze the behavior of different plasma parameters along the white line at $x = 365.5\ d_i$ in Figure 2(a) containing the maximum value of $P_{\mathrm{dyn},x} \sim 90\ n_0 V_A^2$ as seen in Figure 2(g). This simulated jet fulfills the observational criteria in Section 1 and exemplified in Figure 1(a).

1. Within the jet $P_{\mathrm{dyn},x}$ exceeds half of the upstream dynamic pressure (horizontal red line in Figure 2(g)). The maximum $P_{\mathrm{dyn},x} \sim 90\ n_0 V_A^2$ located at $x = 47.5\ d_i$ is
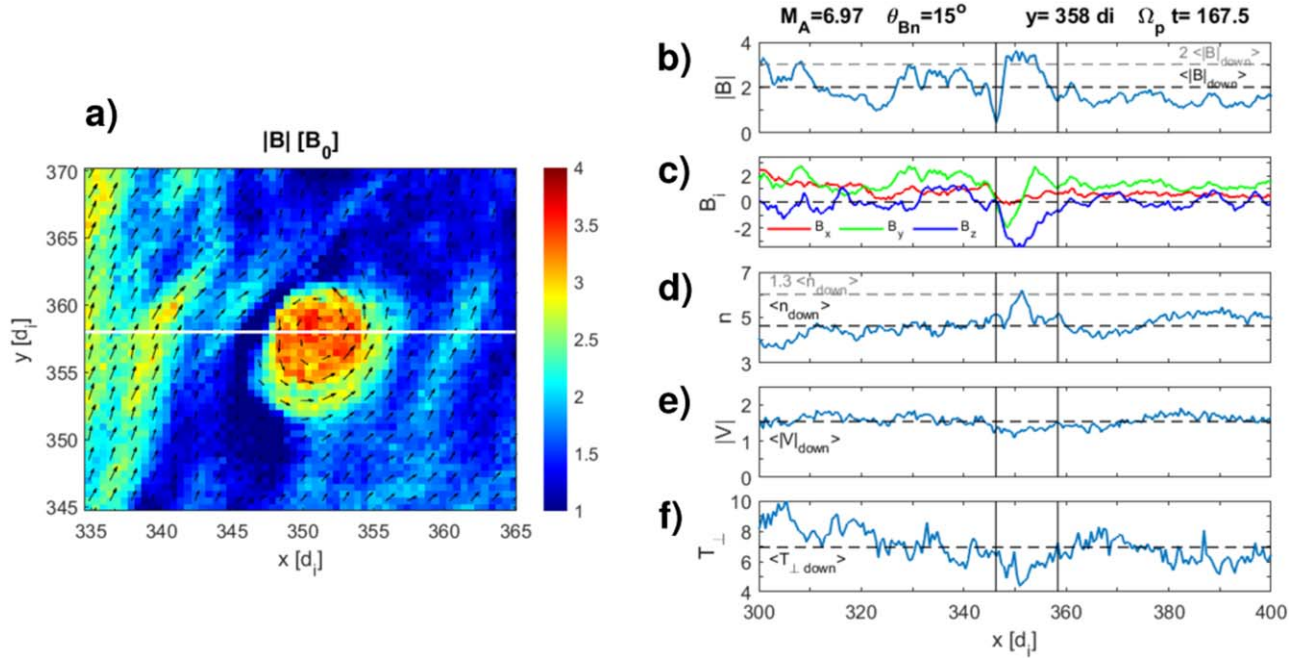
Figure 3. (a) B-field magnitude (colors) and direction (vectors) at $\Omega_p t = 167.5$ for a downstream region of the simulation box. The white line indicates the cut through the plasmoid along which the following spatial profile parameters are plotted: (b) B-field magnitude (averaged downstream values corresponding to $|B|$ and $2|B|$ in black and gray), (c) B-field components, (d) ion density (averaged downstream values corresponding to n and $1.3n$ in black and gray), (e) ion bulk velocity (averaged downstream value in black), and (f) perpendicular temperature (averaged downstream value in black). The vertical lines in the right panels identify the boundary of the plasmoid defined as the local minimums around the B-field magnitude peak.

2.6 times greater than the upstream value. The jet spatial width (between the first and third vertical lines) is approximately 16 d_i, which corresponds to 1600 km assuming a typical d_i value in the upstream region of ~100 km, in agreement with the values between 1200 and 7000 km found by Plaschke et 9l. (2013).

2. Inside the jet, the ion bulk velocity in the x-direction (red trace in Figure 2(f)) is positive, which is equivalent to the anti-sunward propagation as required by Plaschke et al. (2013).

3. Additionally, an increment in ion density (Figure 2(d)) and magnetic field magnitude (Figure 2(b)) inside the jet interval are present.

Figure 3(a) shows a snapshot at $\Omega_p t = 167.5$ of a different region of the simulation box. The colors represent the B-field magnitude, while the black arrows indicate its direction. The shock position is not seen because it is located at $x \sim 300 \, d_i$. A circular structure with a larger magnetic field ($\sim 3.2 \, B_0$) compared with the surroundings can be identified. The B-field vectors inside this structure present rotation in the counter-clockwise direction. We examine different plasma parameters along the white line in Figure 3(a) at $y = 358 \, d_i$. The ion density (Figure 3(d)) shows an increase ($n \sim 6 \, n_0$) inside the structure. We define the boundaries of the structure as the locations of local minimum of the B-magnitude as shown in Figure 3(b). The characteristics listed below fulfill the observational signatures of paramagnetic embedded plasmoids defined in Section 1 and illustrated in Figure 1(b).

1. The ion density enhancement at $x \sim 252 \, d_i$ reaches 1.3 times the averaged density value in the downstream region (Figure 3(d)).

2. The increment in B-field magnitude exceeds twice the average value in the downstream region (Figure 3(b)).

3. The magnetic field components inside the plasmoid exhibit smooth rotations (Figure 3(c)).

4. Velocity values are similar to those in the ambient plasma (Figure 3(e)).

5. There is a decrease in perpendicular temperature compared to the downstream average value (Figure 3(f)).

3.2. Formation Mechanisms

In order to study the formation and evolution of the identified jet and plasmoid, we show in Figures 4 and 5 some snapshots of parts of the simulation domain at different times.

The evolution of the jet is presented in Figure 4 where rows show snapshots of different parameters inside the same region at $\Omega_p t = 90, 92.5, 95$. From left to right the colors on the panels represent $P_{dyn,x}$, proton density, V_x component of bulk velocity and B-field magnitude. In all panels the plasma velocity vectors are superimposed. The rippled shock transition can be identified by the clear increase of B-field magnitude and density and the decrement in $P_{dyn,x}$ and V_x around $x \sim 360 \, d_i$. In the upstream side and along the rippled shock front, the plasma flow is directed approximately parallel to the x-axis. At $\Omega_p t = 90$ immediately downstream of the shock $P_{dyn,x}$ is already somewhat enhanced ($y \sim 345$–$360 \, d_i$) compared to the surrounding downstream plasma. The initially horizontal flow then evolves at $\Omega_p t = 92.5 \, d_i$ to a converging and high-velocity plasma downstream of the now more concave part of the ripple that allows the enhancement of local plasma density and the growth of the region with enhanced $P_{dyn,x}$ that extends further downstream. By $\Omega_p t = 95$ a clear structure with high $P_{dyn,x}$ due to the corresponding increments in density and velocity in x-direction is created and detached from the shock front. At the downstream edge of the jet the plasma flow seems to diverge. The jet signatures are not clear on the panels showing the B-field magnitude. However, we can see that the jet forms between the shock front
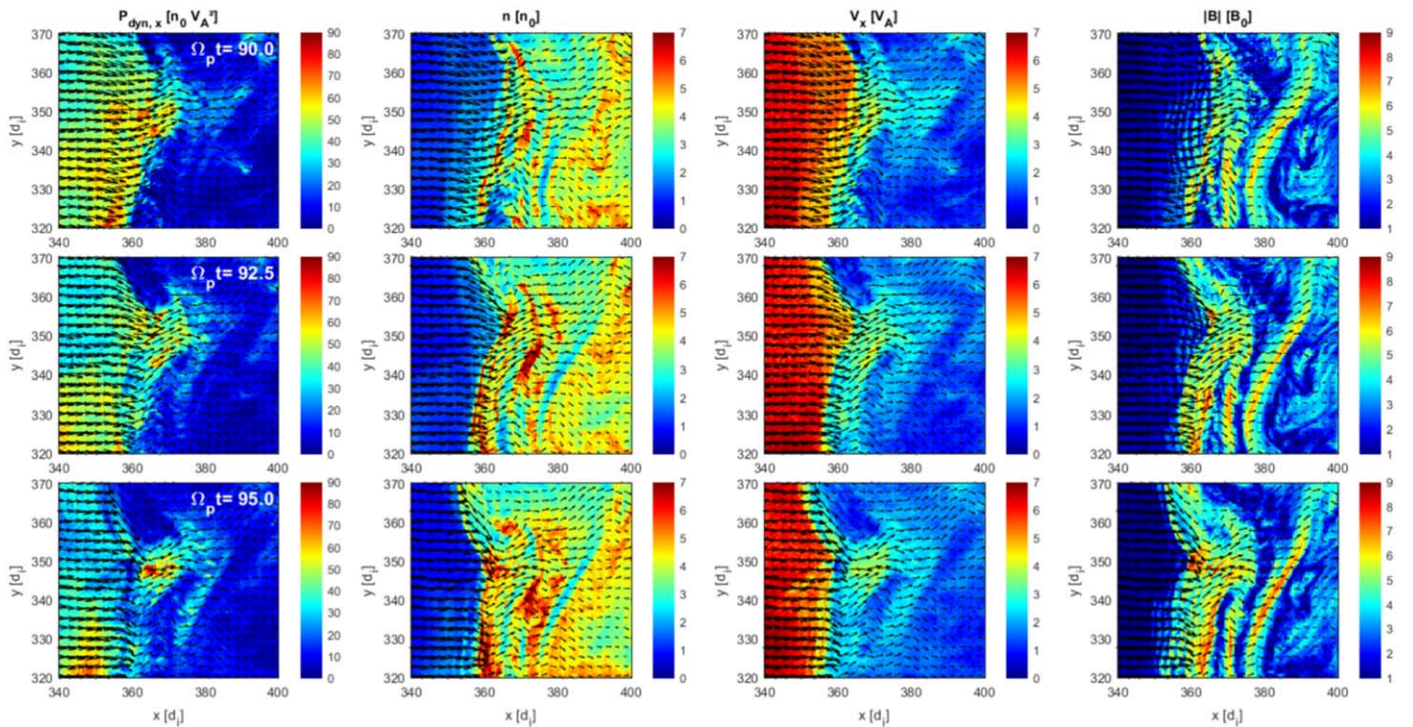
Figure 4. From left to right, isocolor snapshots of $P_{dyn,x}$, proton density, V_x component of bulk velocity, and B-field magnitude. Bulk velocity vectors are superimposed. The different times (rows) correspond to $\Omega_p t = 90, 92.5, 95$ and show the evolution of the shock ripple which gives rise to the formation of the jet reported in Figure 2 in agreement with Hietala et al. (2009).

and a filament of enhanced B, which corresponds to the peak from a previous shock reformation cycle (Burgess 1989, 1995; Scholer & Burgess 1992; Su et al. 2012; Hao et al. 2017). Due to the diverging plasma flow at the downstream edge of the jet at Ω_p $t = 95$, the region of enhanced B-field spreads but it does not coincide with the enhanced $P_{dyn,x}$ region of the jet.

The formation of the plasmoid is presented in Figure 5, where plots show a region of the simulation domain at $\Omega_p t = 95, 105, 112.5, 117.5$. Intermediate times can be examined in Figures A1 and A2 in the Appendix. The colors from left to right in the panels represent plasma density, B-field magnitude, B_y magnitude colored according to its positive (fading red) or negative (fading blue) direction, and B-field magnitude and direction (white arrows) inside the fixed white square on the first three columns. The shock front is identified by the abrupt jump in plasma density and B-field magnitude. Unlike the jet formation mechanism, the evolution of the plasmoid occurs over a longer period of time ($\Omega_p t > 10$). The plasmoid starts to form just behind the shock at $\Omega_p t = 95$ when two layers of plasma, product of shock reformation, having opposite B_y magnetic fields are brought together. By Ω_p $t = 105$ as can be identified in the panel corresponding to enlarged view of B-field an elongated and deformed "U"-shaped red structure with an aligned magnetic field is formed in the region at $x \sim 355-365 \, d_i$ and $y \sim 340-350 \, d_i$. At Ω_p $t = 112.5$ this structure continues to travel to the downstream region shrinking as the legs of the "U" approach each other. By Ω_p $t = 117.5$ the B-field vectors already show a counter-clockwise loop, indicating that reconnection has closed the magnetic loop. As the simulation evolves by $\Omega_p t = 130$ (see Figures A1 and A2 in the Appendix), the plasmoid can be easily identified on density and B panels. This magnetically confined density bump is convected downstream with the surrounding plasma. The fact that the plasmoid stays in the

same location ($x \sim 355 \, d_i$) from the early stages of formation corroborates the embedded nature of the plasmoid, namely that it is transported with the downstream flow. The plasmoid stays embedded throughout its existence (see Figures A1 and A2 in the Appendix), which lasts until $\Omega_p t \sim 200$.

4. Discussion and Conclusions

In this work we present a simulation study where we reproduce the observational signatures of a magnetosheath jet and a paramagnetic embedded plasmoid. We show for the first time that these structures are formed by different mechanisms. For the paramagnetic embedded plasmoid the formation mechanism has not been previously proposed. In this sense, and for the parameters of the simulation similar to those found at the bow shock, jets and plasmoids can be considered as different entities in both their properties and formation mechanisms.

The formation of the simulated jet follows the mechanism proposed by Hietala et al. (2009) along the rippled quasi-parallel shock interface, that is, at the ripple where the shock normal and the flow velocity are not parallel, the incident plasma is less decelerated and more deflected than the surrounding material leading to a local concurrence of material in the downstream region. Both features produce the formation of the enhanced $P_{dyn,x}$ structure that we identified as the jet. Our results differ from those recently found in an hybrid simulation by Hao et al. (2016a), who did not observe the focusing effect mentioned by Hietala et al. (2009), although they did observe increased B-field magnitude along its filamentary jet. More-over, their mechanism includes a downstream secondary shock as an obstacle that allows the deflection of the flow in the downstream region. The discrepancies between our results and theirs can be due to the differences in their simulation setup (e.g., $\theta_{Bn} = 30°$ and $M_A = 5.5$).
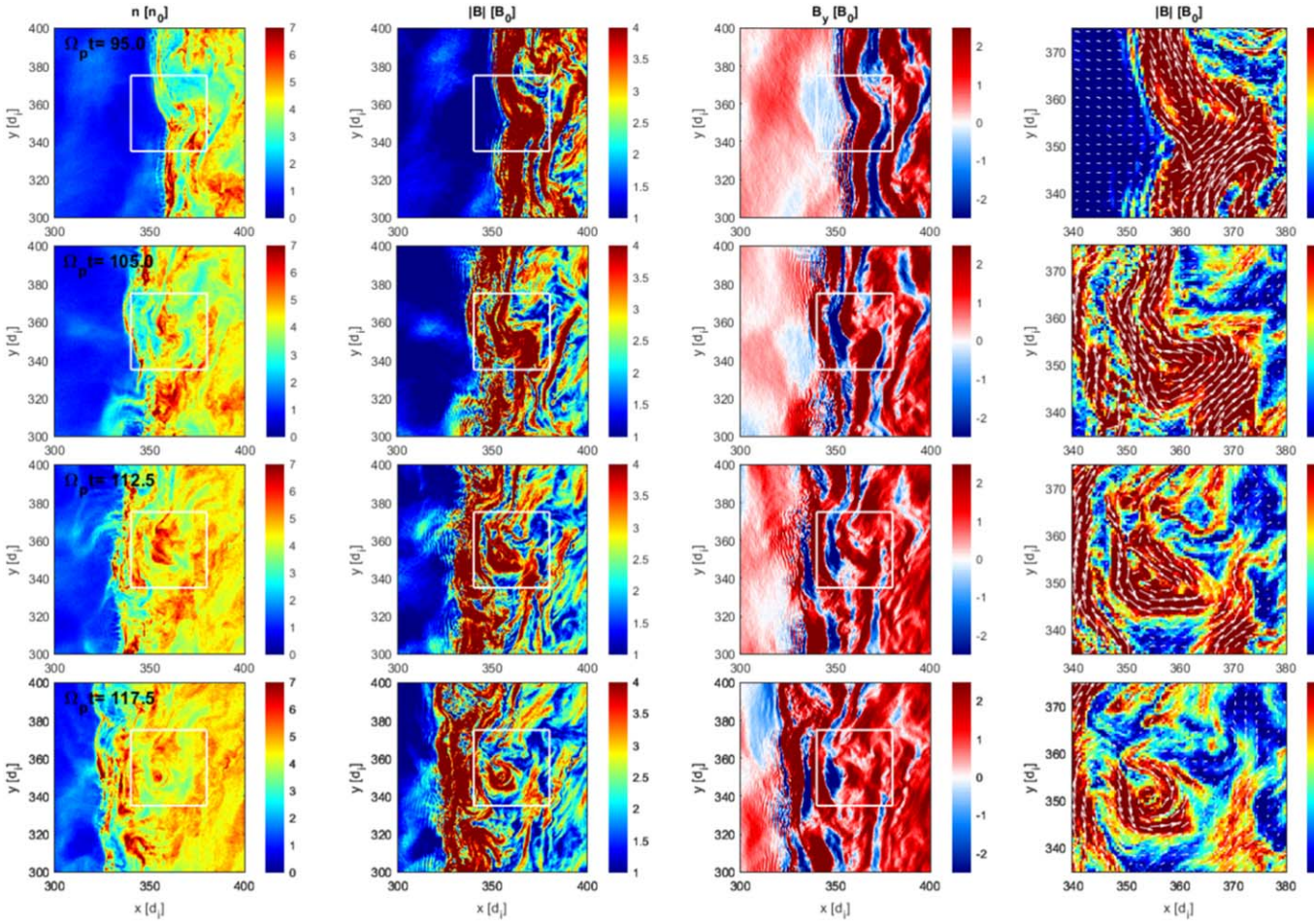
Figure 5. From left to right, isocolor snapshots of ion density, B-field magnitude, B_y magnitude colored according its positive (fading red) or negative (fading blue) direction, and B-field magnitude (isocolors and vectors) in the region delimited by the white square. The different times (rows) corresponds to $\Omega_p t = 95, 105.0, 112.5, 117.5$ and show the evolution of the shock region where the plasmoid ($\Omega_p t = 117.5$) is formed and which will evolve to that reported in Figure 3(a). The extended formation timeline is shown in Figures A1 and A2 in the Appendix.

On the other hand, the simulated plasmoid is formed at the immediate downstream region by the magnetic reconnection of two opposite B_y-oriented plasma layers that are piling up behind the shock due to the local reformation process characteristic of quasi-parallel shocks (Hao et al. 2016a, 2017). This mechanism gives rise to the formation of a B-field loop, which detaches the plasma inside it from the surroundings, allowing its transport with the downstream. This is the first time that this mechanism is suggested for the formation of paramagnetic embedded plasmoids characterized observationally by Karlsson et al. (2012, 2015). Shock reformation that can be due to upstream waves, shocklets, and SLAMS is then crucial because as these no linear magnetic structures pile up at the shock and become part of the downstream region where the B-field fluctuates rapidly, they change its orientation by up to 180° across small distances. Such large shear angles between the plasma layers provide the ideal conditions for the onset of magnetic reconnection, which eventually leads to the formation of plasmoids.

It is then clear how the different formation mechanisms of jets and paramagnetic embedded plasmoids also can explain some of the differences between their signatures: the magnetically confined nature of the plasmoid is responsible for its high density compared with the surroundings by isolating the plasma inside it inhibiting its diffusion as it is transported downstream. In contrast, the increment

in density observed inside some jets is explained by the focusing effect at the ripple, which also increase the V_x component in the same region producing the bump in $P_{\mathrm{din},x}$. Also, due to its embedded nature the paramagnetic plasmoid does not present an increase in velocity and its life time is longer than that of the jet, so it would be more easily found away from the shock front compared to the jet.

These novel results have interesting implications in the context of recent works (Karlsson et al. 2015; Plaschke et al. 2018), which suggest that paramagnetic embedded plasmoids can be regarded as a subset of magnetosheath jets because both present a local increase in $P_{\mathrm{dyn},x}$ (see Figure 1). Although the two structures found in the simulation do share this characteristic, clearly it is not produced by the same mechanism.

Our work shows how numerical simulations can be used as a powerful tool to study different aspects of downstream structures. These results could be applied/contrasted to interpret the observational magnetosheath high-resolution data provided by different multi-spacecraft missions (e.g., Magnetospheric Multiscale (MMS), Cluster, and Time History of Events and Macroscale Interactions during Substorms (THEMIS)) and serve as motivation for future observational and theoretical studies. Future simulation work will include the analysis of VDFs, temperature anisotropy, and particle tracking inside and around simulation jets and

plasmoids as well as the study of these structures with fully 3D simulations.

Appendix
Plasmoid Formation Mechanism: Additional Plots

Here we present more snapshots for the simulated output timesteps covering the formation of the studied plasmoid reported in Figure 3. The format of the figures is the same as the reported in Figure 5. Although here we only show the time interval $95 \leqslant \Omega_p t \leqslant 170$, the structure of the plasmoid, that is its internal magnetic rotation and increase in density, persist until $\Omega_p t \sim 200$ as well as its position at $x \sim 350\ d_i$.
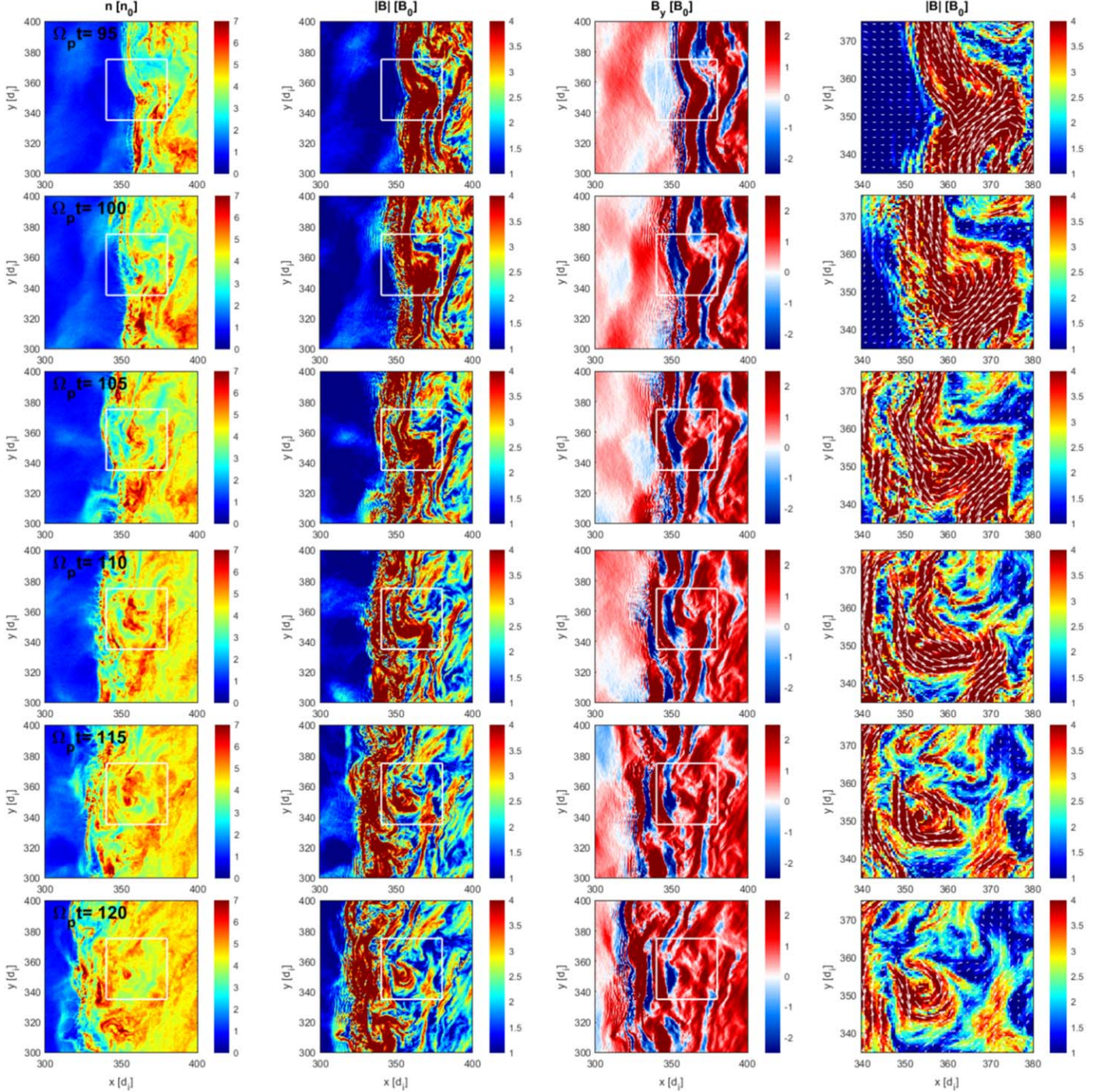
Figure A1. Isocolor snapshots corresponding (left to right) to ion density, B-field magnitude, B_y magnitude colored according its positive (fading red) or negative (fading blue) direction, and B-field magnitude (isocolors and vectors) in the region delimited by the white square. The timeline evolution (top to bottom) corresponds to $\Omega_p t = 95, 100, 105, 110, 115, 120$.
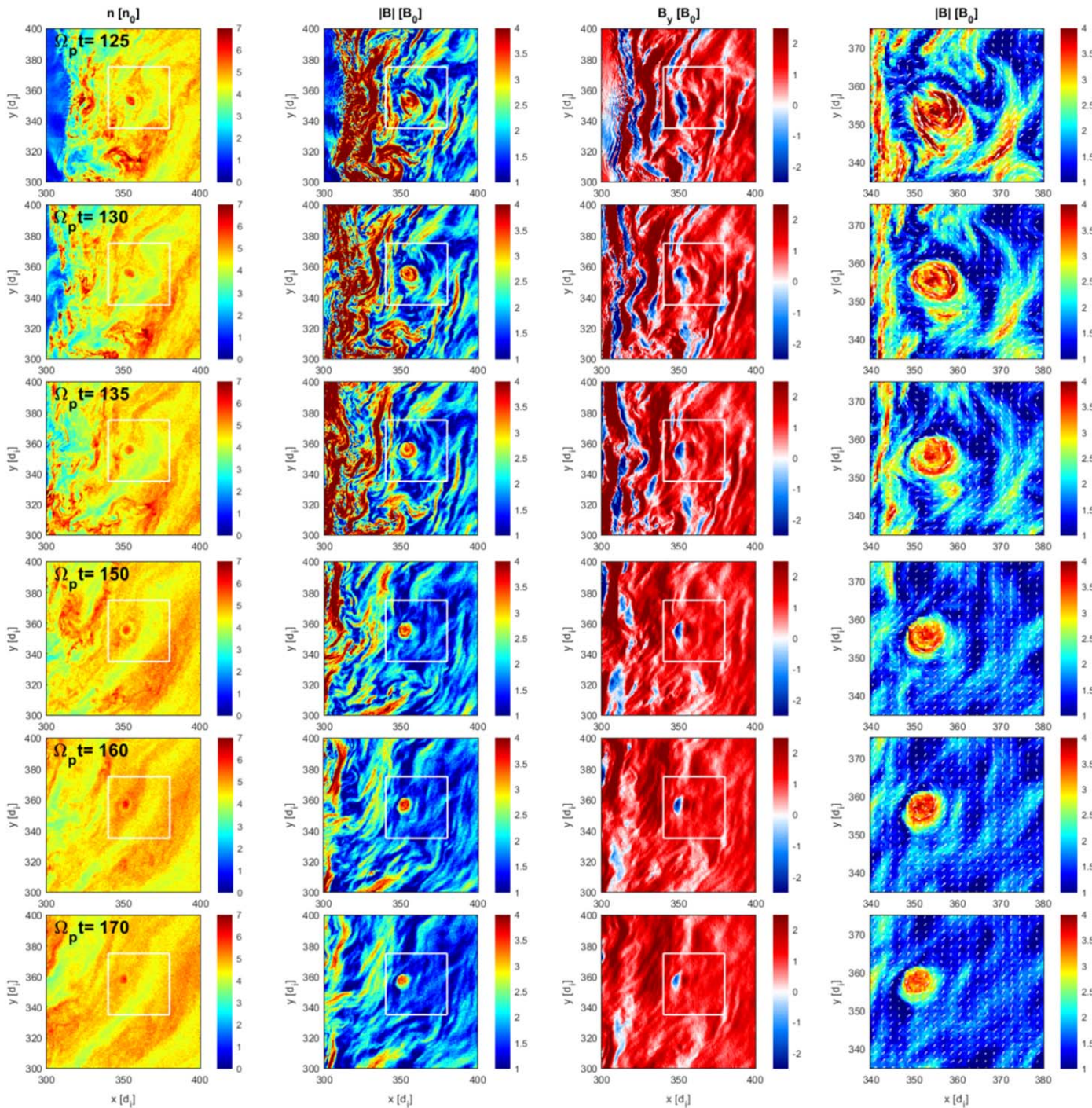
Figure A2. Same format as in Figure A1, now corresponding to $\Omega_p\, t = 125, 130, 135\ 150, 160, 170$.

ORCID iDs

Luis Preisser https://orcid.org/0000-0002-5636-2014
Xóchitl Blanco-Cano https://orcid.org/0000-0001-7171-0673
Primoz Kajdič https://orcid.org/0000-0002-0625-8892
David Burgess https://orcid.org/0000-0002-8175-9056
Domenico Trotta https://orcid.org/0000-0002-0608-8897

References

Amata, E., Savin, S. P., Ambrosino, D., et al. 2011, P&SS, 59, 482
Archer, M. O., & Horbury, T. S. 2013, AnGeo, 31, 319
Archer, M. O., Horbury, T. S., & Eastwood, J. P. 2012, JGR, 117, A05228
Blanco-Cano, X., Omidi, N., & Russell, C. T. 2009, JGRA, 114, A01216
Burgess, D. 1989, GeoRL, 16, 345
Burgess, D. 1995, AdSpR, 15, 159
Burgess, D. 1995, Collisionless Shocks (Cambridge: Cambridge University Press), 129
Burgess, D., & Scholer, M. 2015, Collisionless Shocks in Space Plasmas: Structure and Accelerated Particles, Cambridge Atmospheric and Space Science Series (Cambridge: Cambridge University Press)
Dubouloz, N., & Scholer, M. 1995, AdSpR, 15, 175
Eastwood, J. P., Balogh, A., Lucek, E. A., Mazelle, C., & Dandouras, I. 2005, JGRA, 110, A11219
Giacalone, J., Schwartz, S. J., & Burgess, D. 1993, GeoRL, 20, 149

Gingell, I., Schwartz, S. J., Burgess, D., et al. 2017, JGRA, 122, 11,003
Gunell, H., Stenberg Wieser, G., Mella, M., et al. 2014, AnGeo, 32, 991
Gutynska, O., Sibeck, D. G., & Omidi, N. 2015, JGRA, 120, 7687
Hao, Y., Gao, X., Lu, Q., et al. 2017, JGRA, 122, 6385
Hao, Y., Lembege, B., Lu, Q., & Guo, F. 2016a, JGRA, 121, 2080
Hao, Y., Lu, Q., Gao, X., & Wang, S. 2016b, ApJ, 823, 7
Hietala, H., Laitinen, T. V., Andréeová, K., et al. 2009, PhRvL, 103, 245001
Hietala, H., Partamies, N., Laitinen, T. V., et al. 2012, AnGeo, 30, 33
Hietala, H., & Plaschke, F. 2013, JGRA, 118, 7237
Hubert, D., & Harvey, C. C. 2000, GeoRL, 27, 3149
Karlsson, T., Brenning, N., Nilsson, H., et al. 2012, JGR, 117, A03227
Karlsson, T., Kullen, A., Liljeblad, E., et al. 2015, JGR, 120, 7390
Krauss-Varban, D., & Omidi, N. 1991, JGR, 96, 17715
Lucek, E. A., Constantinescu, D., Goldstein, M. L., et al. 2005, SSRv, 118, 95
Lucek, E. A., Horbury, T. S., Balogh, A., Dandouras, I., & Rème, H. 2004, JGRA, 109, A06207
Němeček, Z., Šafránková, J., Přech, L., et al. 1998, GeoRL, 25, 1273
Omidi, N., O'Farrell, A., & Krauss-Varban, D. 1994, AdSpR, 14, 45
Omidi, N., & Sibeck, D. G. 2007, JGRA, 112, A01203
Plaschke, F., Hietala, H., & Angelopoulos, V. 2013, AnGeo, 31, 1877
Plaschke, F., Hietala, H., Archer, M., et al. 2018, SSRv, 214, 81
Rakhmanova, L. S., Riazantseva, M. O., Zastenker, G. N., & Verigin, M. I. 2018, Ge&Ae, 58, 718
Savin, S., Amata, E., Budaev, V., et al. 2014, JETPL, 99, 16
Savin, S., Amata, E., Zelenyi, L., et al. 2012, AnGeo, 30, 1
Scholer, M., & Burgess, D. 1992, JGR, 97, 8319
Schwartz, S. J., & Burgess, D. 1991, GeoRL, 18, 373
Schwartz, S. J., Burgess, D., & Moses, J. J. 1996, AnGeo, 14, 1134
Schwartz, S. J., Burgess, D., Wilkinson, W. P., et al. 1992, JGR, 97, 4209
Shevyrev, N. N., & Zastenker, G. N. 2005, P&SS, 53, 95
Shevyrev, N. N., Zastenker, G. N., Nozdrachev, M. N., et al. 2003, AdSpR, 31, 1389
Su, Y., Lu, Q., Gao, X., Huang, C., & Wang, S. 2012, PhPl, 19, 092108
Tsubouchi, K., & Lembège, B. 2004, JGRA, 109, A02114
Tsurutani, B. T., & Stone, R. G. 1985, in Collisionless Shocks in the Heliosphere: Reviews of Current Research, Geophysical Monograph Ser, Vol. 35, ed. B. T. Tsurutani & R. G. Stone (Washington DC: AGU), 7
Yordanova, E., Vörös, Z., Varsani, A., et al. 2016, GeoRL, 43, 5969